Sustainable Energy & Fuels

ROYAL SOCIETY OF CHEMISTRY

PAPER

View Article Online
View Journal | View Issue

Cite this: *Sustainable Energy Fuels*, 2025, **9**, 2031

Metal-free graphitic carbon nitride/carbon-dots composites: unveiling mechanochemical synthesis opportunities†

Ilaria Bertuol,‡[a] Lucía Jiménez-Rodríguez,‡[b] Rafael R. Solís,[b] Patrizia Canton,[a] Maurizio Selva,[a] Mónica Calero,[b] Alvise Perosa,[a] Daily Rodríguez-Padrón*[a] and Mario J. Muñoz-Batista*[b]

Environmentally friendly, metal-free photocatalysts offer a promising alternative to traditional metal-based semiconductors. In this study, we synthesised graphitic carbon nitride (CN) photocatalysts decorated with carbon dots (CDs) using two distinct methods: a hydrothermal approach and a solvent-free mechanochemical extrusion method. The resulting nanocomposites were thoroughly characterised for their physical, chemical, and optical properties and evaluated for photocatalytic activity in the selective oxidation of benzyl alcohol. Results revealed that the synthetic approach significantly impacted the composites' morphological and optical characteristics, affecting their photocatalytic performance. A light–matter interaction modelling study was further conducted to explore the relationship between optical properties and catalytic behaviour, offering valuable insights into the structure–function relationship of these novel photocatalysts. As a result, we present an alternative scheme to traditional synthesis and catalysis methods based on the use of high temperature and pressure conditions, which provides an energetically positive and environmentally friendly approach.

Received 13th February 2025
Accepted 11th March 2025

DOI: 10.1039/d5se00220f

rsc.li/sustainable-energy

1 Introduction

Carbon dots (CDs), defined as spherical-like carbon particles,[1] are an emerging class of nanomaterials characterized by their unique optical properties, biocompatibility, low toxicity and highly functionalized surface, involving hydroxyl, carboxyl and amine groups. CDs combine many of the advantageous features of traditional Quantum Dots (QDs), such as resistance to photobleaching and size- and wavelength-dependent luminescence, with superior biological properties, including high aqueous dispersibility.[2]

Notably, CDs can be synthesized inexpensively and on a large scale, often through a one-step process using biomass waste-derived sources, positioning them as a sustainable alternative to conventional fluorescent materials and toxic metal-based QDs.[3] Two main approaches for CDs synthesis can be highlighted: top-down and bottom-up. The top-down approach breaks down larger carbon materials through chemical, electrochemical, or physical methods.[4,5] In contrast, the bottom-up approach involves the thermal decomposition of organic precursors through techniques like pyrolysis, hydrothermal methods, and microwave-assisted processes.[6] The latest method allows more precise control over the composition and structure of the CDs, being often preferred for its simplicity and ability to fine-tune nanomaterial properties.[7,8]

CDs features, which are intimately linked to their core–shell composition and size,[9] make them highly attractive for a wide range of applications, including bioimaging and biosensing, photocatalysis, design of optoelectronic devices, antibacterial treatments, self-healing materials, and security technologies, among others.[10] Particularly in photocatalysis, CDs show great promise for enabling sustainable, cost-efficient metal-free catalytic processes in reactions such as oxidation, oxidative cleavage, reduction, isomerization, substitution, condensation, and polymerization.[11,12] One of the earliest reports on CDs for photocatalysis was published in 2020.[13] This piece of research explored CDs with varying crystallinities, both with and without nitrogen doping, and tested their effectiveness as photocatalysts in the reductive methylene–oxygen bond cleavage of *N*-methyl-4-picolinium esters. Similar CDs were also tested in the photoreduction of methyl viologen, where nitrogen functionalities on the surface and the amorphous nature of the CDs were found to enhance photocatalytic activity.[9]

However, despite these promising advantages, CDs face significant challenges, particularly in their practical application as photocatalysts. One of the most pressing issues is the

[a]*Department of Molecular Science and Nanosystems, Ca' Foscari University of Venice, Via Torino 155, 30175 Venezia Mestre, Italy. E-mail: daily.rodriguez@unive.it*
[b]*Department of Chemical Engineering, University of Granada, 18074 Granada, Spain. E-mail: mariomunoz@ugr.es*

† Electronic supplementary information (ESI) available. See DOI: https://doi.org/10.1039/d5se00220f

‡ These authors have contributed equally to this work.

difficulty in recovering CDs after a catalytic reaction, which limits their reusability and increases operational costs, rendering them a "single-use" catalyst.[14] This challenge has spurred research into new strategies to enhance the practicality and efficiency of CDs in photocatalytic systems.

A promising approach to overcome this limitation involves the incorporation of CDs into carbonaceous materials,[15] such as graphitic carbon nitride (CN).[16] CN is a well-known photocatalyst, recognized for its layered structure, thermal stability, and suitable bandgap (2.7 eV) for visible light absorption. Despite its promising catalytic activity, CN also faces challenges related to weak van der Waals interactions between adjacent CN layers, which hinder charge transfer and separation, thereby limiting its photocatalytic efficiency. By supporting CDS on CN, it is possible to create composite materials that combine the strengths of both components. These composites can enhance photocatalytic performance through improved charge separation, and extended light absorption, thus making them more efficient and versatile in various photocatalytic applications.[17] CDs, whose π–π conjugated structure is similar to CN, have been effectively used as light absorbers in combination with semiconductor nanoparticles like TiO_2, SiO_2 and Ag_3PO_4.[18–21] This combination not only improves photocatalytic performance but also enables CDs to act as electron acceptors or transporters, directing the flow of photogenerated charge carriers. Consequently, the synergy between CDs and CN is expected to deliver enhanced photocatalytic performance, making this combination a promising avenue for future applications.[22]

Various methods for synthesizing CN/CDs composites have been explored in the literature. Traditional approaches often involve solution-based processes, such as hydrothermal or solvothermal methods, or thermal treatments that promote the integration of CDs with CN. Despite their effectiveness, these methods present some limitations, such as requiring harsh conditions or complex procedures, and the use of solvents and additional reagents, which could harm the environment.[23]

As a result, there is growing interest in alternative synthesis methods, such as mechanochemistry, which offers a green, solvent-free, and energy-efficient approach to material preparation. Mechanochemistry, which relies on mechanical force to drive chemical reactions, is particularly relevant for the synthesis of nanomaterials.[23] It can potentially facilitate the formation of strong interactions between CDs and CN, leading to composite materials with enhanced photocatalytic properties. The relevance of mechanochemistry in the synthesis of carbon-based composites relies not only on their environmental benefits but also on their potential to produce materials with superior structural and functional characteristics, which are crucial for advanced photocatalytic applications. To the best of our knowledge, mechanochemistry, particularly reactive extrusion, has not been reported for the preparation of graphitic carbon nitride/carbon dots (CN/CDs) composites.

In this study, we synthesized a series of composite materials based on CN and CDs using two different bottom-up approaches: a conventional hydrothermal method and mechanochemical extrusion. The photocatalytic activity of these nanomaterials was tested in the oxidation of benzyl alcohol to benzaldehyde, a key reaction relevant to lignocellulosic biomass valorisation. This investigation also provides insights into the structure–activity relationship, the impact of the synthetic method, and the light–matter interaction through a modelling study.

2 Experimental

All chemicals employed during the reactions and the synthesis of catalysts were commercially available compounds sourced from Sigma-Aldrich. If not otherwise specified, reagents and solvents were employed without further purification.

2.1. Synthesis of catalytic materials

2.1.1 CDs. Two types of nitrogen-doped CDs were synthesised using two different approaches, namely pyrolysis and hydrothermal synthesis, using citric acid as the carbonaceous source and urea as the N-containing precursor.

Graphitic N-doped CDs (g-CDs) were synthesized by a pyrolysis procedure. A mixture of citric acid (10.0 g) and urea (5.0 g) was heated at 220 °C for 48 h in a conical flask equipped with a distillation apparatus. The crude was then collected and dried under reduced pressure, obtaining a dark-brown solid in 50 wt% yield. Part of the crude product, referred to this work as g-CDS (nd), was used for the preparation of catalytic composites without further purification. The remaining solid was then dialyzed against milliQ water (2 L) for 24 h using a 1 kDa MWCO dialysis bag, changing the water every 6 h. The pure dark solid product, referred to here as g-CDs(d), was obtained in 8 wt% yield.

Amorphous N-doped CDS (a-CDS) were synthesized by hydrothermal treatment of citric acid (1.0 g) and urea (0.5 g) in MilliQ water (25 mL). The mixture was put into a PTFE-lined autoclave reactor and heated at 180 °C for 6 h. The product was then filtered and dried under reduced pressure, resulting in the a-CDs as a brownish powder reaching roughly 70 wt% yield.

CN was prepared by a simple pyrolysis method with a 28 wt% yield. Melamine (5.0 g) was put into a quartz cylinder and treated at 550 °C under a nitrogen atmosphere for 3 h. After pyrolysis, the sample was ultrasonically treated in 90 mL of deionized water for 30 min at room temperature.

2.1.2 Composite catalytic materials. The CN/CDs composite materials were synthesized, in a second step, following two different approaches, namely mechanochemistry through extrusion and a hydrothermal protocol (Table 1).

2.1.2.1 Mechanochemistry through extrusion method. The materials were synthesized using CN (1.0 g), CDS (0.1 g), and Milli-Q water (1 mL). The mixture was extruded in a ZE 12 HMI Twin-Screw Extruder (Three Tec, Seon, Switzerland) at a temperature of 120 °C and a speed of 50 rpm, for 1 h of residence time. The extrudate was collected without further purification.

2.1.2.2 Hydrothermal method. Hydrothermal synthesis was performed adapting a reported procedure.[24] 0.1 g of CDs were ultrasonicated in 10 mL of Milli-Q water for 15 min. Thereafter, 1.0 g of CN dispersed in 90 mL of Milli-Q water, and the

Table 1 Composite catalytic materials.[a,b]

Sample name	Description
CN	Carbon nitride made from melamine
e-CN/a-CDs	Composite materials obtained by extrusion
e-CN/g-CDs(nd)	
e-CN/g-CDs(d)	
h-CN/a-CDs	Composite materials obtained
h-CN/g-CDs(nd)	by hydrothermal treatment
h-CN/g-CDs(d)	

[a] nd = non dialysed; d = dialysed. [b] e = obtained by extrusion; h = obtained by hydrothermal treatment.

previously mentioned CDs dispersion were mixed and stirred at room temperature for 30 min. Subsequently, the mixture was transferred into a PTFE-lined autoclave reactor and heated to 120 °C for 4 h. The precipitate was collected, washed three times with distilled water, centrifuged at 6000 rpm for 10 min and dried at 70 °C under reduced pressure overnight.

2.2. Characterisation of catalytic materials

The crystalline structure of the samples was investigated by X-ray diffraction (XRD) in a D8 Advance diffractometer from Bruker® AXS, using the X-ray source of the Cu Kα radiation, coupled to a LynxEye detector, and monitoring the 2θ within 8–80° at a rate of 0.08° min^{-1}.

The chemical composition on the surface of the solids was examined using X-ray Photoelectron Spectroscopy (XPS) with a Physical Electronics VersaProbe II Scanning XPS Microprobe. This equipment uses a monochromatic X-ray Al-Kα radiation source under a vacuum of 10^{-7} Pa. The binding energies were calibrated to the C 1s peak from adventitious carbon at 284.8 eV. High-resolution spectra were recorded using a concentric hemispherical analyser at a constant energy pass of 29.35 eV over a 200 μm diameter analysis area. The pressure in the analysis chamber was maintained below 5×10^{-6} Pa. Data acquisition and analysis were performed using PHI ACCESS ESCA-F V6 software. A Shirley-type background was subtracted from the signals, and the recorded spectra were analysed with Gauss–Lorentz curves to determine the binding energy of the atomic levels of different elements more accurately.

The textural properties were determined from N_2 physisorption at −196 °C, performed in a Syn 200 instrument from 3P Instruments. The samples were outgassed at 110 °C under vacuum for 12 h in a J4prep station from 3P Instruments. The specific surface area was calculated by the BET method; the pore volume from N_2 uptake at $p/p_0 \sim 0.99$. The pore size distribution was estimated using the Barrett, Joyner and Halenda (BJH) method.

Transmission electron microscopy (TEM) was performed to observe the size and shape of the particles in a JEOL 2010 operated at an acceleration voltage of 200 kV and with a FEI Tecnai G2 system, equipped with a charge-coupling device (CCD) camera. Samples were ground and then suspended in ethanol, followed by dipping of a holey-carbon coated copper grid of 300 mesh which was dried under air for a few minutes before recording.

2.3. Photocatalytic experiments

The photocatalytic behaviour of the prepared samples was assessed in the selective oxidation of benzyl alcohol (BA) to produce benzaldehyde (BZ). As shown in Fig. 1, the photocatalytic experiments were conducted in a jacketed cylindrical photoreactor, in whose centre two UVA (365 nm, 9 W each) lamps were placed. The reacting slurry suspension (catalyst dose, 0.5 g L^{-1}) was pumped through the annular space. The temperature was controlled at 20 °C with the help of an auxiliary tank containing the alcohol solution (1 mM), which was

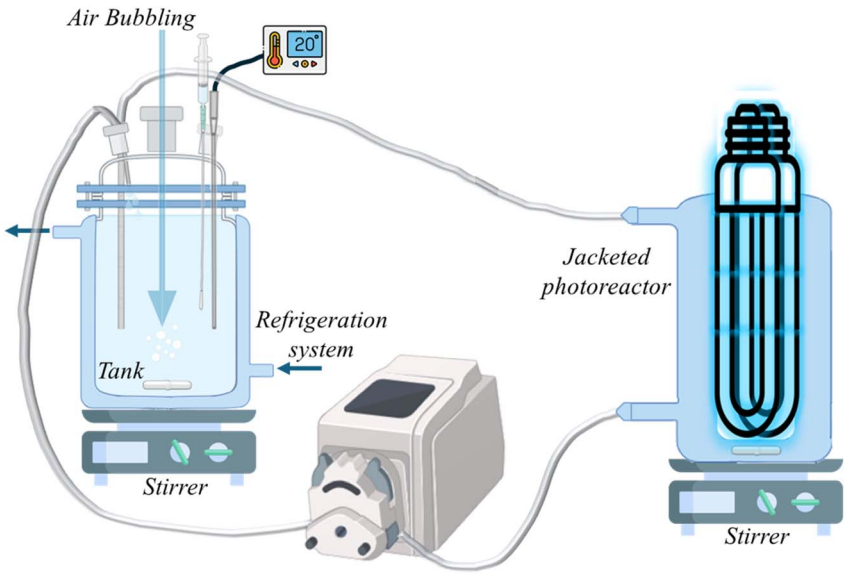

Fig. 1 Schematic representation of the photoreactor setup.

pumped to the annular space of the photoreactor. To ensure the presence of dissolved O_2, air was supplied in the auxiliary tank. Before starting the photocatalytic assay, an adsorption period was conducted in dark conditions to ensure the adsorption equilibrium. Next, the lamps were switched on, samples were withdrawn and filtered (Millex PVDF, 0.45 μm) before analysis. The influence of the oxidative species was evaluated by adding chemical scavengers that suppress certain reactive routes during the oxidation of the alcohol to the aldehyde. The role played by superoxide radical was tentatively analysed by exchanging air with N_2 bubbling, or the presence of specific inhibitors such as *p*-benzoquinone (1 mM) or disodium 4,5-dihydroxybenzene-1,3-disulfonate (tiron, 1 mM). The addition of *tert*-butyl alcohol (TBA, 10 mM) was considered to remove the action of the hydroxyl radicals.

High-Pressure Liquid Chromatography (HPLC) technique was used for quantifying the concentration of the alcohols and the aldehydes. The HPLC device was an Alliance 2695 HPLC from WatersTM, with a 2998 photodiode Array detector. A Zorbas Bonus-RP column (5 μm, 4.6 ×150 mm) was used. The pumped mobile phase (1 mL min^{-1}) was a mixture of 40% (v/v) acetonitrile and 60% (v/v) ultrapure water acidified with 0.1% (v/v) of trifluoroacetic acid. The wavelength selected for quantification was 215 nm for BA and 248 nm for BD. The activity was evaluated in terms of initial reaction (pseudo-first order) rate and quantum efficiency (eqn (1)). The selectivity (S) of the BZ was calculated from the aldehyde and alcohol temporal profiles. The quantum efficiency (Q_E) of BA photo-degradation was estimated, following the IUPAC's recommendations which defines the Q_E as the ratio of the number of molecules reacting through the reaction rate ($r_{BA,0}$), by the photon absorption rate (LVRPA, $e^{\alpha,\nu}$).[25] The ESI† provides a detailed description of the procedure for determining the $e^{\alpha,\nu}$ (see light–matter interaction modelling section). The solution of the light–matter interaction model is based on solving the Radiative Transfer Equation (RTE) for the reactor geometry using two-dimensional, two-directional radiation approach.[26,27] As described in the ESI,† the determination of the optical properties of the catalytic suspension was also estimated from the solution of the Radiative Transfer Equation (RTE) using a one-dimensional, one-directional radiation model for the spectrophotometer cell.[28]

$$Q_E = \frac{r_{CA_0}(\text{mol m}^{-3}\ \text{s}^{-1})}{e^{\alpha,\nu}(\text{einstein per m}^3\ \text{per s})} \quad (1)$$

3 Results and discussion

3.1. Synthesis of CN/CDs composite materials

Through this work, the synthesis of CN/CDs composite materials has been explored, using two distinct and sustainable approaches: a conventional hydrothermal method and mechanochemical extrusion (Fig. 2). These methods were chosen not only for their environmental advantages but also for their potential to produce high-performance materials in a scalable manner. The hydrothermal method, known for its ability to generate well-defined nanostructures under mild conditions, offers a controlled environment where temperature and pressure facilitate the formation of materials with tailored properties.[29] This approach is particularly appealing due to its simplicity and the use of water as a solvent, aligning with green chemistry principles by reducing the need for harmful reagents and minimizing waste. On the other hand, mechanochemical extrusion represents an innovative, solvent-free technique. This method is gaining attention for its ability to synthesize materials with unique properties that are often difficult to achieve through traditional solution-based methods.[30] Mechanochemistry, by reducing or even eliminating the need for solvents, contributes significantly to the sustainability of material synthesis. Moreover, its capacity to scale up production, especially through extrusion, while maintaining consistency in material properties makes it an attractive option for industrial applications. By employing these two methods, our work aims to understand how different synthetic procedures influence the physical, chemical and optical properties of CN/CDs composites.

3.2. Characterization of CN/CDS composite materials

The textural properties of the synthesized samples were assessed through N_2 physisorption, focusing on how porosity and surface area are affected by different synthetic methodologies. The materials produced *via* extrusion and hydrothermal

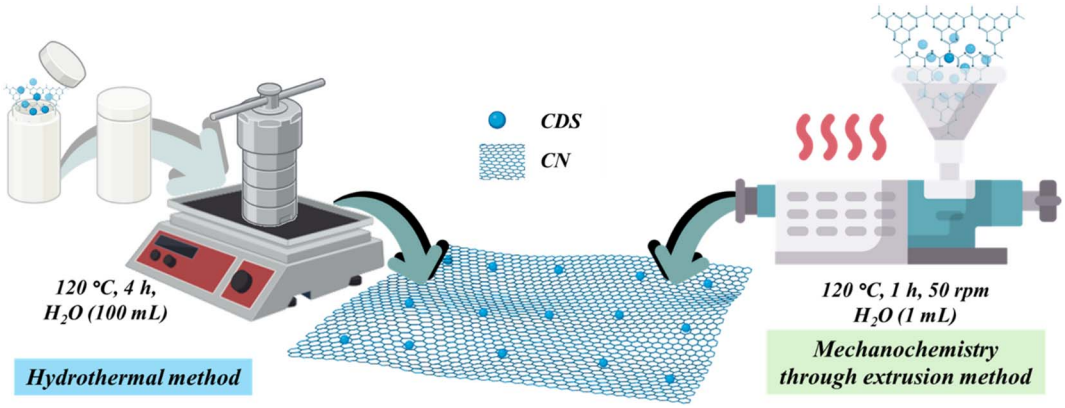

Fig. 2 Schematic representation of the synthetic protocols employed for the preparation of the composite photocatalytic materials.

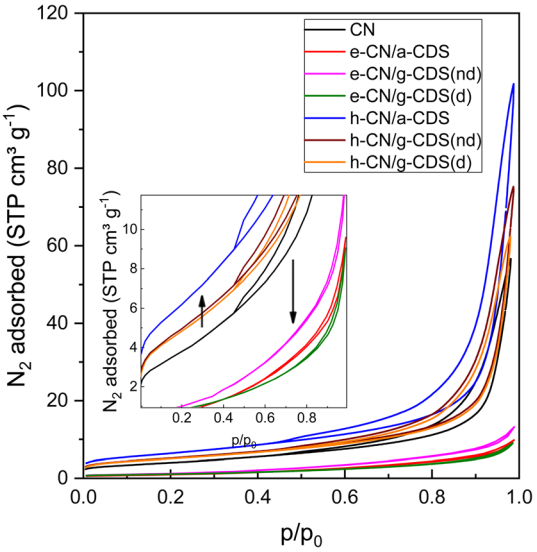

Fig. 3 Nitrogen adsorption–desorption isotherms at 77 K for the studied materials. The inset shows the details of the isotherms' differences as a function of the preparation method.

methods were compared to the unmodified graphitic carbon nitride. Fig. 3 illustrates isotherms fitting the Type II, according to IUPAC classification,[31] describing the typical shape of low porous material with high contribution of mesopores. As shown in Table 2, all samples exhibit average mesopore diameter values ranging from 17.3 to 27.6 nm. Type H3 hysteresis loops were observed, typically associated with aggregates of plate-like particles forming slit-shaped pores.[32,33] In general, the mechanochemical approach resulted in a reduction in mean pore size, pore volume, and surface area. This suggests that the high-energy mixing and compression involved in extrusion may lead to a denser material with less developed porosity, which could potentially offer benefits in terms of material stability and durability, depending on the specific application.[34] Conversely, the hydrothermal method yielded samples with relatively higher surface areas, larger pore sizes, and greater pore volumes, compared to the unmodified CN, which could have significant implications for their performance in catalytic applications.[35–37] Overall, these findings suggest that the choice of synthetic method plays a crucial role in determining the textural properties of CN/CDs composites.[38]

The XRD diffractograms of the composite samples, presented in Fig. 4A, and the CN reference for comparison purposes, displayed two key peaks. The prominent peak around 27°, corresponds to the (002) plane and is indicative of the interlayer spacing in the graphitic structure of CN. The smaller peak near 13°, corresponding to the (100) plane, provides information about the in-plane periodicity of the atomic arrangement within the individual layers.[39] This reflection is associated with the repeating structure of tri-*s*-triazine motifs within the CN sheets. In the three synthesized samples *via* the hydrothermal method, the peak at 27° remained sharp and well-defined, indicating that the CN retained its crystalline structure. Conversely, in the three mechanochemical extrusion samples, the (002) peak showed noticeable broadening. This broadening is indicative of an increase in structural disorder, likely due to the high-energy mechanical forces applied during the extrusion process.[40]

Fig. 4B shows the FT-IR spectra of the four representative CN/CDs composite samples alongside the reference graphitic carbon nitride, with all spectra displaying identical characteristic signals. These signals correspond to the typical vibrational modes of CN, indicating that its fundamental chemical structure was preserved in the composite materials. The prominent bands observed between 1200 and 1600 cm^{-1} can be attributed to the stretching vibrations of C–N and C=N bonds within the aromatic heterocycles, characteristic of the graphitic carbon nitride framework.[41] Additionally, the sharp peak around 810 cm^{-1} corresponds to the out-of-plane bending vibrations of the tri-*s*-triazine units, further confirming the presence of intact CN structures in all samples.[42] The similarity in the FT-IR spectra across the composite samples suggests that the incorporation of CDs into the CN matrix did not significantly alter the chemical structure of the carbon nitride. This consistency in the spectral features suggests that the CDs are well-dispersed within the CN matrix without disrupting its covalent network.

Fig. 5(5A–C) shows the XPS results for the C 1s, N 1s, and O 1s regions of the composite systems and the CN reference, alongside with the corresponding proposed fittings (5D–5F) of the composite sample e-CN/g-CDs(d). From the analysis of the C 1s region (Fig. 5A) a contribution at 284.6 eV due to C–C bonds,[43] is clearly visible in all cases, but it is significantly higher in all composite materials if compared to unmodified CN.[44,45] From the corresponding fitting in Fig. 5D well-defined

Table 2 Textural properties and bandgap of the samples[a]

Samples	S_{BET} (m^2 g^{-1})	V_T (cm^3 g^{-1})	D_{BJH} (nm)	Bandgap (eV)
CN	13.8	0.088	25.4	2.70
e-CN/a-CDS	3.0	0.015	19.8	2.59
e-CN/g-CDS(nd)	4.0	0.020	20.0	1.26
e-CN/g-CDS(d)	3.2	0.014	17.3	1.65
h-CN/a-CDS	22.4	0.155	27.6	2.71
h-CN/g-CDS(nd)	18.0	0.116	25.8	2.61
h-CN/g-CDS(d)	17.3	0.097	22.4	2.54

[a] S_{BET}: specific surface area was calculated using the Brunauer–Emmett–Teller (BET) equation. D_{BJH}: mean pore size diameter was calculated using the Barret–Joyner–Halenda (BJH) equation. V_T: total pore volume from the N_2 uptake at $p/p_0 \sim 0.99$.

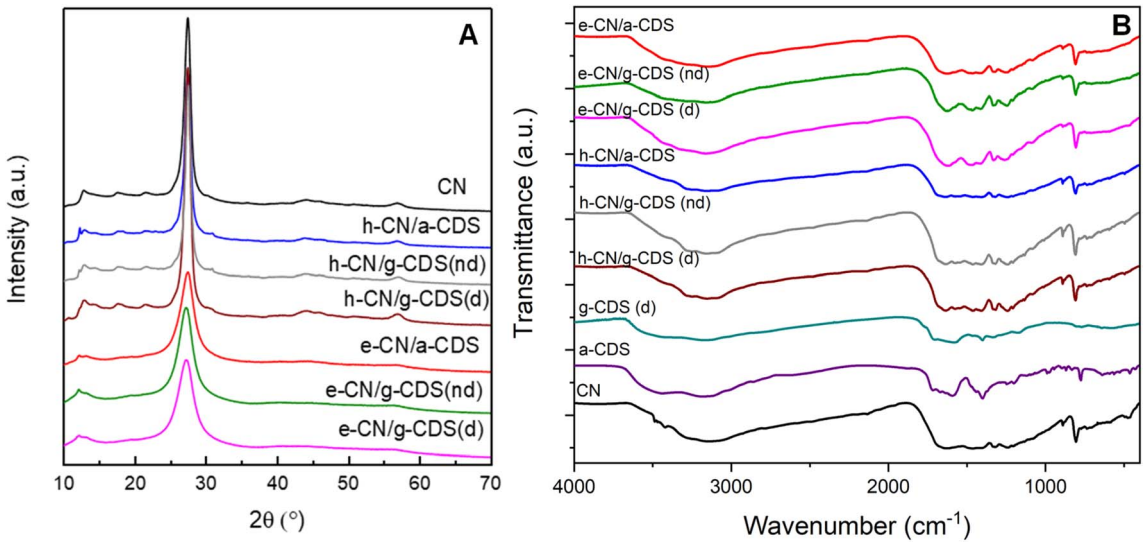

Fig. 4 (A) XRD patterns and (B) FT-IR spectra of representative catalytic systems.

peaks can be associated to the C–N bond, and the C–$(N)_3$ group, respectively.[43] These contributions are characteristic of the triazine structure of CN, where carbon is primarily bonded to nitrogen within the graphitic network. The signals at 286.0 and 287.0 eV, corresponding to C–O and C=O bonds, are primarily attributed to oxygenated functionalities on the CDS surface,

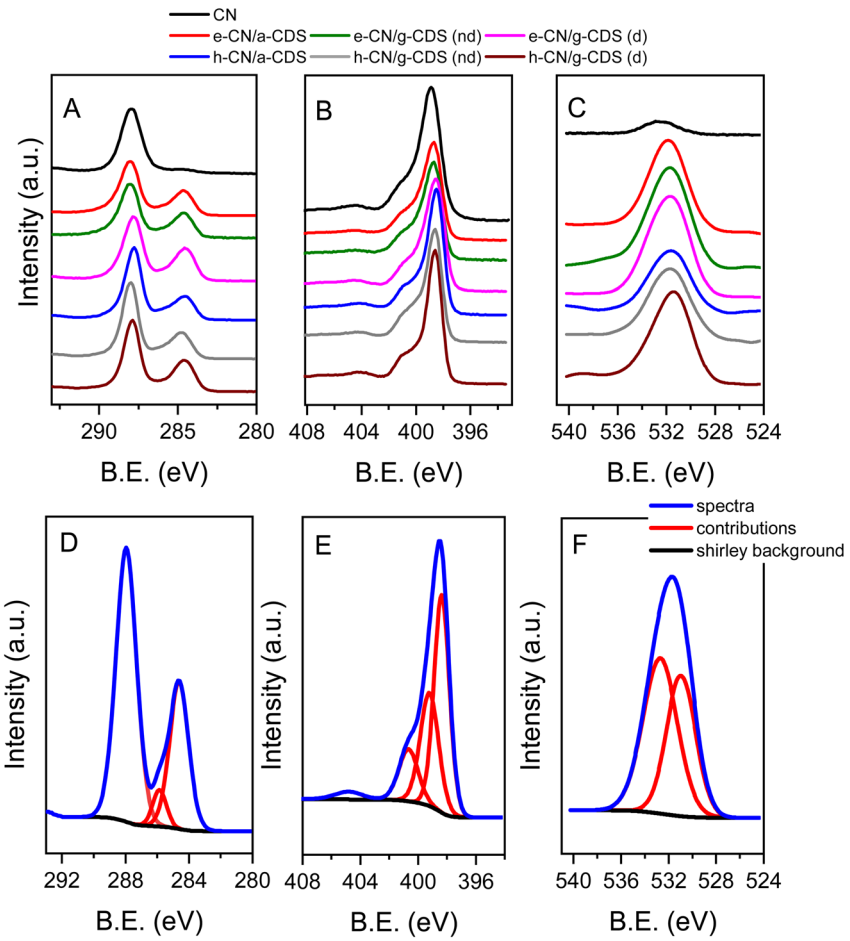

Fig. 5 XPS results corresponding to the (A) C 1s, (B) N 1s, and (C) O 1s regions. Proposed fitting (D–F) for the e-CN/g-CDS(d) sample.

with a possible contribution from surface oxidation. The XPS analysis of the N 1s region provides further insight into the chemical environment of nitrogen in both the reference CN and the CN/CDs composites (Fig. 5B). As shown in Fig. 5E, the first peak, located at approximately 398.5 eV, is attributed to the C–N=C bonds, typically characteristic of sp^2-hybridized nitrogen within the triazine rings of CN.[43] At around 400.0 eV, a contribution related to N–$(C)_3$, representing nitrogen atoms bonded to three carbon atoms in a tertiary amine configuration is considered. This peak reflects the nitrogen atoms at the edges of the triazine units or within defects in the CN structure. A smaller peak near 401.0 eV is typically assigned to protonated nitrogen species, such as N–H, which may result from surface interactions with atmospheric moisture or during the synthetic process.[43] The XPS O 1s region spectra presented in Fig. 5C, reveal that the pure CN exhibits a less intense band compared to the CN/CDs composites. This low intensity suggests that pure CN has minimal surface oxidation and fewer oxygen-containing groups. In contrast, the composites exhibit a more pronounced peak in the O 1s spectrum, indicating a significant increase in surface oxygen functionalities due to the presence of carbon dots (*i.e.* C–O/C=O). As presented in Fig. 5F, both C–O and C=O contributions were found placed at 532.4 and 530.0 eV, respectively. This enhanced peak intensity reflects the successful introduction of oxygenated groups with the carbon dots. The analysis of the atomic percentages of carbon, nitrogen, and oxygen, as well as the C/N, O/N, and O/C ratios obtained from XPS are summarized in Table S1† of the ESI.† The C/N ratio remains relatively stable across all composite samples, ranging from 1.03 to 1.25. For the reference CN, the C/N ratio is 0.81 which is in line with a well-defined CN structure.[43] The slight variations in the ratio (C/N > 1) for composites are consistent with the incorporation of carbon dots, which can introduce additional carbon while maintaining the nitrogen-rich triazine structure CN. The sample h-CN/g-CDS(d) shows the highest C/N ratio (1.25), indicating an enhanced carbon contribution in the system. The O/C ratio shows a more pronounced variation, reflecting the extent of oxygenated groups in the samples. A similar trend was observed for the O/N ratio. The reference CN shows a ratio of 0.04, indicating a nitrogen-rich structure with minimal oxygen. The addition of carbon dots, especially the dialyzed ones, significantly increases this ratio. In the mechanochemically prepared samples, the O/C ratio rises to 0.13–0.14, while the hydrothermal method yields a maximum of 0.15 for h-CN/g-CDS(d). This suggests that, as expected, carbon dots introduce oxygenated functional groups in all samples, but the presence of oxygen-related functional groups is maximized by combining the hydrothermal synthesis and the use of purified carbon dots.

TEM analysis has also been performed to further investigate the morphology of the synthesised materials and verify the incorporation of CDs (Fig. 6 and S1–S3 of the ESI†). Fig. 6 shows a representative TEM image of the h-CN/g-CDs(d) photocatalytic sample. It is worth to mention that, given the inherent low

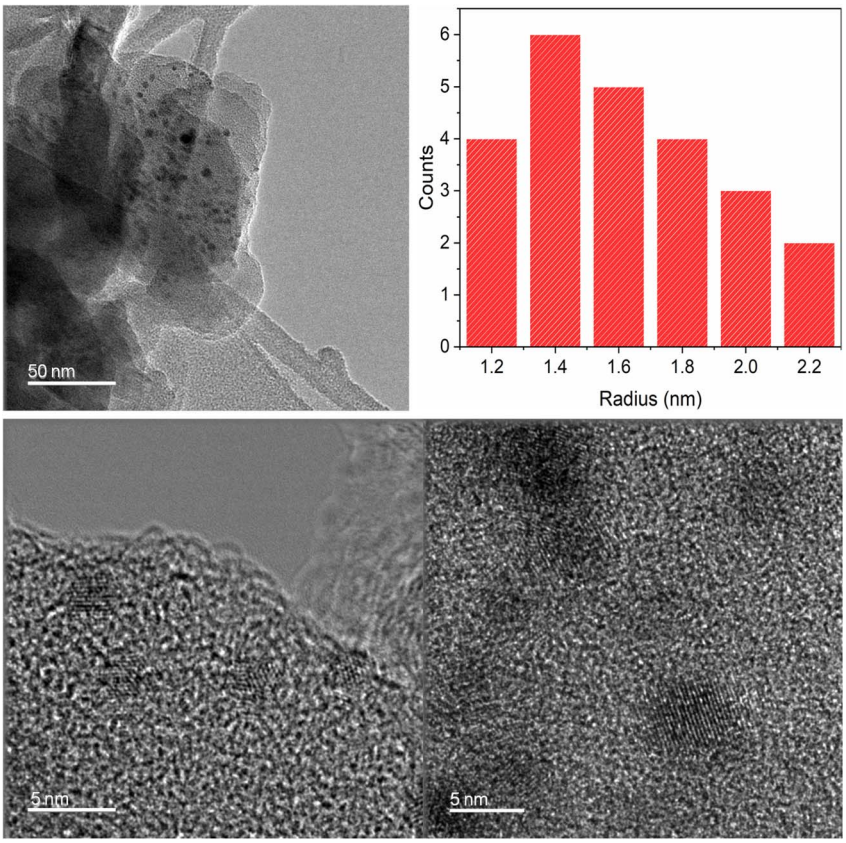

Fig. 6 HR-TEM micrograph of the h-CN/g-CDs(d) photocatalytic sample.

contrast between carbon dots and the graphitic carbon nitride matrix, identifying individual CDs presents a significant challenge. To maximize accuracy in their visualization, we carefully selected regions where particle distinction was most reliable. While analyzing a larger area could improve statistical representation, the contrast limitations would compromise the clear identification of CDs. The micrograph reveals that the particles are predominantly spherical and uniformly dispersed across the surface of the CN matrix. The particle size distribution was relatively narrow, with most particles ranging from 1.2 to 2.2 nm and an average diameter of 1.4 nm, as illustrated in the inset size histogram. High-resolution TEM further confirmed the crystalline nature of these carbon particles and the formation of a layered structure associated with the CN, which is consistent with the typical architecture of the graphitic carbon nitride framework.[46]

This contribution presents a rigorous analysis of the optical properties based not only on DRS-UV-vis measurements (Fig. 7A) but also on a strict determination of local volumetric photon absorption profiles (Fig. 7B–I), calculated from the modelling of light–matter interactions.[47,48] As shown in Fig. 7A, the reference sample CN exhibits a typical profile with absorption occurring in the UV region and extending into the visible part, enabling the determination of a bandgap value of 2.7 eV.[49] The composite materials obtained through extrusion and hydrothermal methods exhibit different trends concerning

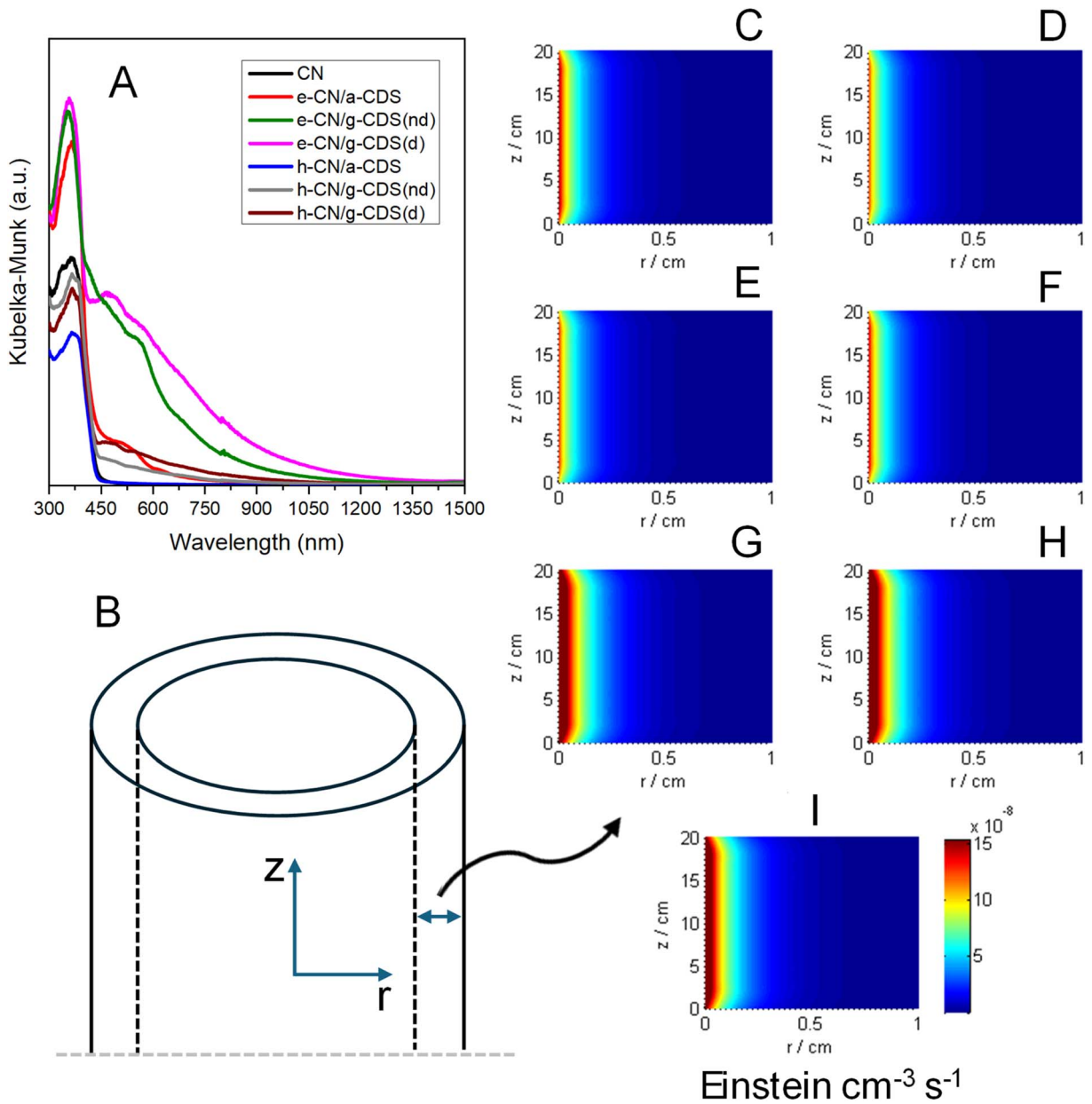

Fig. 7 (A) UV-visible spectra of the CN reference and the CN/CDs composite materials. (B) Schematic description of coordinate system in which the LSRPA is represented. Local volumetric rate of photon absorption (einstein per cm^3 per s) for (C) pristine-CN, (D) h-CN/a-CDs, (E) h-CN/g-CDs(nd) (F) h-CN/g-CDs(d), (G) e-CN/a-CDs, (H) e-CN/g-CDs(nd), (I) e-CN/g-CDs(d).

their absorption properties. The series obtained *via* the hydrothermal method shows less variation in terms of Bandgap modification. The CN modified with a-CDS (amorphous species) did not display any change in the Bandgap value, whereas a slight reduction was observed for the samples produced by the hydrothermal method with the g-CDs. The reduction of the bandgap becomes more pronounced when the g-CDs are dialyzed. In contrast, the variation the bandgap is observable in the series obtained by mechanochemistry must be highlighted. As observed in Fig. 7A, the mechanochemical approach provides structures which lead to the appearance of a shoulder, detectable in all samples obtained through extrusion. The shoulder above 450 nm may arise from several factors related to the incorporation of CDs. Firstly, it could be attributed to the formation of new localized energy states within the bandgap of CN introduced by the carbon dots.[50] These states can act as intermediate energy levels, facilitating electronic transitions at lower energies, thereby extending the absorption spectrum into the visible range. Furthermore, the intense mechanical forces involved in mechanochemistry can disrupt the crystalline order of CN, leading to increased surface defects, such as nitrogen vacancies, edge dislocations, and unsaturated bonds. These defects create local electronic states within the bandgap of CN, which can facilitate additional electronic transitions, contributing to the absorption band above 450 nm.[51] In contrast, the hydrothermal method tends to produce more crystalline and uniform materials with fewer defects.[52] As a result, the electronic structure of hydrothermally synthesized CN is less altered, and the optical absorption of pristine CN is maintained.

Fig. 7B describe the defined coordinate system for which the Photon Absorption is calculated. Fig. 7C–I depicts the photon absorption profiles of the composite systems, and the reference CN expressed in Einstein per cm^3 per s. The shape of the absorption profiles is similar for all samples and is determined by the geometry of the reaction system (annular reactor and symmetrically positioned illumination system at the centre of the reactor). As expected, the direction associated with the z-coordinate shows minimal variations for each evaluated radius (r-coordinate), with a slight reduction attributed to what is commonly referred to as the edge effect (defined by the lamp dimension in that coordinate).[26] From the position $r = 0$ (the first layer of liquid receiving radiation), a drastic reduction in the absorption profile is detected. Fig. 7C shows the absorption profile for the reference CN. Fig. 7D–F depict the profiles corresponding to the series obtained *via* the hydrothermal method. The profiles demonstrate that using this method, the optical properties of the suspension remain without significant variations in comparison to the unmodified CN (LVRPA values approximately equal to $1.4–1.6 \times 10^{-8}$ einstein per cm^3 per s^1). In contrast, the photon absorption profiles for the samples obtained *via* mechanochemistry (Fig. 7G–I) show a considerable increase compared to the pure CN reference (2.6×10^{-8} einstein per cm^3 per s^1), which indicates an enhancement of UV light absorption. Similar values of LVRPA among amorphous, crystallized, and dialyzed carbon dots prepared using the same synthesis method, suggest that the primary factor influencing the absorption rate is the synthesis method itself rather than the treatment of the CDS. In practical reaction conditions (using an irradiation source of 365 nm), as reflected by the LVRPA calculation, the optical properties are defined by the structural and electronic properties induced by the synthesis method rather than by the treatment of the CDs. Mechanochemical synthesis may lead to enhanced photon absorption due to increased defect density in the CN, which overshadows any differences introduced by CDS treatment. Conversely, as aforementioned, hydrothermal synthesis produces a more uniform CN structure, resulting in similar absorption rates across different CDs treatments.

3.3. Photocatalytic activity of CN/CDs composite materials in the benzyl alcohol oxidation reaction

The photocatalytic results are illustrated in Fig. 8A and B (reaction rate and selectivity to benzaldehyde). In the samples prepared through extrusion, the amorphous CDs, with high surface defect density, may strongly interact with the defect-rich CN matrix, promoting more efficient charge transfer and higher reaction rates. In turn, dialyzed graphitic CDs, although less defective than amorphous ones, still contribute to higher reaction rates, in comparison with the non-dialyzed CDs most likely due to the interaction of molecular fluorophores or impurities retained in the CDs before dialysis with the organic reactants. On the one hand, the hydrothermal synthesis, with a similar trend to the amorphous-related sample, showed the highest reaction rate, followed by the dialyzed one. On the other hand, quantum efficiency is identified as a more critical metric for evaluating photocatalytic performance.[48] Although mechanochemically prepared samples exhibit a higher LVRPA, the quantum efficiency data clearly show that this does not directly result in improved quantum efficiency. The quantum efficiency represents the efficiency of absorbed photons to be converted into reactive species, and it is influenced by several factors not limited to optical properties.[53] This suggests that the optimization of both optical properties and surface chemistry is essential for achieving high photocatalytic performance. The effective utilisation of absorbed photons, driven by favourable charge carrier dynamics and surface interactions, is crucial for maximizing the photocatalytic activity of CN/CDs composites. However, in selective synthesis applications, such as the partial oxidation of benzyl alcohol to benzaldehyde, the purification and stabilization of carbon dots on the CN surface are expected to enhance selectivity. A selectivity of approximately 60% for benzaldehyde is achieved, indicating that while amorphous a-CDs provides certain advantages, stabilization and purification are critical for optimizing selectivity in the reaction. No other organic intermediates were detected in the reaction products, confirming that CO_2 and H_2O are the sole by-products resulting from the complete mineralization of the alcohol. The optimization of the benzaldehyde production can be undertaken considering that the purification by dialysis typically removes smaller, non-covalently bound impurities and residual solvents from the carbon dots.[54] This purification can lead to a more uniform surface and a reduction in potential quenching

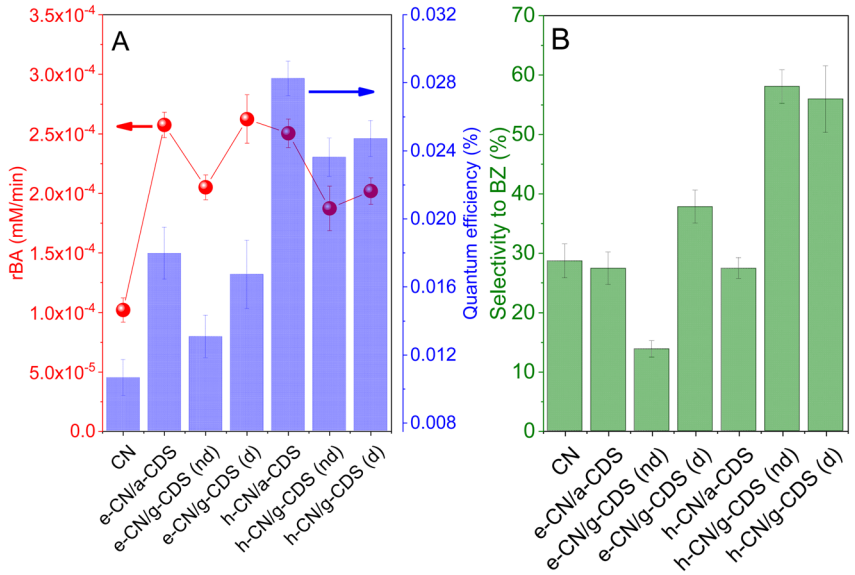

Fig. 8 (A) Reaction rate (pseudo-first order) and quantum efficiency, and (B) selectivity to benzaldehyde of composite samples and CN reference.

sites or other interactions that could interfere with the photocatalytic process. The cleaner surface, with a more homogeneous structure, the better control of the photoactive sites for effective aldehyde production.

3.4. Mechanistic investigations of the photocatalytic oxidation of benzyl alcohol using CN/CDs composite materials

A tentative analysis of the mechanism of selective benzaldehyde production based on reactions with different scavengers was developed (Fig. 9A). There is no complete and exclusive inhibition by the most popularly used scavengers and their addition may alter the adsorption equilibria; however, this strategy leads to a global understanding of the oxidative routes with a major contribution. The sample with the highest quantum yield from each series was selected, namely e-CN/a-CDs and h-CN/a-CDs. The influence of the superoxide radical ($O_2^{\bullet-}$) was analysed using three reaction schemes; eliminating O_2 from the reaction medium by bubbling N_2, adding *p*-benzoquinone (*p*-BZQ), or disodium 4,5-dihydroxybenzene-1,3-disulfonate (tiron). One of the major pathways for superoxide radical ($O_2^{\bullet-}$) formation is through the reduction of molecular oxygen. This process, driven by photogenerated conduction band electrons, is crucial for producing reactive oxygen species that facilitate oxidation reactions in photocatalysis. Removing O_2 from the medium by bubbling N_2 blocks this pathway, significantly lowering the generation of $O_2^{\bullet-}$, altering the recombination effect though. *p*-Benzoquinone (*p*-BZQ) is commonly used in scavenger studies in photocatalysis due to its high reactivity with $O_2^{\bullet-}$,[55] while tiron has been recognized as a more reliable alternative since hinders some side reactions that *p*-BZQ promotes in a photocatalytic medium.[56,57] It is evident, as shown in Fig. 9A, that the removal of oxygen by bubbling nitrogen in the media leads to significant reductions in quantum efficiency. Specifically, the quantum efficiency decreased by a factor of 9.7 for h-CN/a-CDs

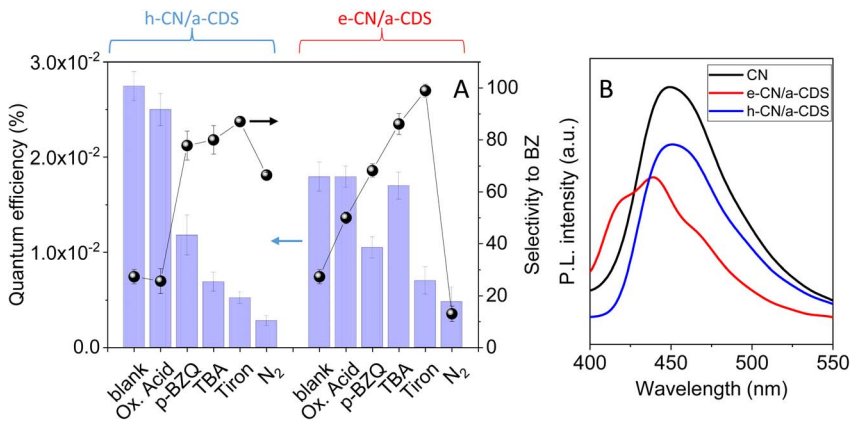

Fig. 9 (A) Quantum efficiency of selected samples using scavengers. (B) PL spectra selected samples and CN reference.

and 3.7 for e-CN/a-CDs. The use of *p*-BZQ and tiron as scavengers further support this, as both compounds trap $O_2^{\bullet-}$. However, a key limitation of scavengers like *p*-BZQ and tiron is their ability to capture not only the target species but also other reactive species, such as hydroxyl radicals ($HO^{\bullet}$), especially in the case of *p*-BZQ.[56] However, the reaction rates for capturing $HO^{\bullet}$ are much lower compared to those for $O_2^{\bullet}$ meaning that even if $OH^{\bullet}$ is being scavenged to some extent, it would be at a significantly lower rate than $O_2^{\bullet}$. The use of *tert*-butyl alcohol (TBA), a known scavenger for $HO^{\bullet}$, provides valuable insight into the influence of this radical during the photocatalytic reaction.[56] In the case of h-CN/a-CDs, the significant reduction in quantum yield upon the addition of TBA suggests that $HO^{\bullet}$ radicals play a crucial role in enhancing the photocatalytic performance of this material. The removal of $HO^{\bullet}$ likely interferes with key oxidative processes, leading to a marked decrease in photocatalytic efficiency. This could indicate that $HO^{\bullet}$ is involved in reactions that promote the oxidation of substrates or facilitate electron–hole pair separation, thus contributing to the overall photocatalytic activity. In contrast, for e-CN/a-CDs, the quantum yield remained largely unaffected by TBA, implying that $HO^{\bullet}$ radicals have a less significant role in the photocatalytic process of this material. This lack of response could suggest that the electron transfer dynamics or the reaction pathways in the extruded sample are less reliant on $HO^{\bullet}$, or that other reactive species, such as $O_2^{\bullet-}$, dominate the photocatalytic process. The formation of hydroxyl radicals $HO^{\bullet}$ is not expected in CN because the holes generated in the valence band have an oxidation potential lower than that required to oxidize water to $OH^{\bullet}$ (+2.31 V *vs.* NHE at pH 7).[58] The use of oxalate as a hole-trapping agent is a common strategy to explore the importance of holes (h^+) in photocatalytic reactions, as oxalate can capture the holes generated in the valence band. The results suggest that the direct attack on the molecule by the holes is negligible, as the use of oxalate as a hole-trapping agent does not significantly affect the quantum efficiency in either sample. Preferentially eliminating $O_2^{\bullet-}$ from the system decreases selectivity toward benzaldehyde, as $O_2^{\bullet-}$ plays a crucial role in facilitating the oxidation of benzyl alcohol to benzaldehyde. However, the increased importance of $HO^{\bullet}$, especially when $O_2^{\bullet-}$ is reduced, can lead to undesired side reactions, as hydroxyl radicals are a less selective oxidant. In this context, $HO^{\bullet}$ can cause overoxidation or the formation of other byproducts, compromising the selective production of benzaldehyde. According to the data, the main photocatalytic mechanism in the e-CN/a-CDs sample is dominated by the superoxide radical $O_2^{\bullet-}$. On the other hand, in the h-CN/a-CDs sample, there is a combined contribution of both $O_2^{\bullet-}$ and $HO^{\bullet}$. However, it is important to note that $HO^{\bullet}$ is not expected to come from the oxidation by the photo-generated holes, but from an alternative pathway such as the protonation of $O_2^{\bullet-}$, leading to the formation of $HO_2^{\bullet}$, which can then decompose into $HO^{\bullet}$ and O_2.[47] In conclusion, both modified formulas seem to prefer the oxidation of the alcohol by superoxide radicals.

A relationship between the optical properties of the samples and the mechanisms described earlier can be stated. The heightened activity in the hydrothermal sample could be related to LVRPA calculations (Fig. 7D–F). The reaction rate of the sample prepared by mechanochemistry is competitive compared to those obtained using the traditional hydrothermal method. However, the quantum yield values are higher in the series produced by the hydrothermal approach. This indicates that, although the hydrothermal series absorbs less radiation (Fig. 7D–I), UV light is sufficient to release the generation of holes and electrons, followed by the subsequent radical mechanism. This enhanced absorption capacity directly correlates with its improved photocatalytic performance under UV irradiation, likely facilitating the generation of reactive species, especially photogenerated holes, in the reaction.

In addition to the involved ROS in the reaction mechanism, it is interesting to assess the recombination effect launched by each sample. Fig. 9B shows the photoluminescence (PL) spectra for both composite samples and the reference (CN) sample, excited at 365 nm. Both composites display a noticeable decrease in PL intensity compared to the CN reference, indicating an efficient charge separation likely due to electron transfer between CN and the CDS, which reduces electron–hole recombination. The extrusion-synthesized sample showed a more significant intensity reduction than the hydrothermal counterpart, suggesting that the extrusion process enhances the electronic interaction between CN and the CDs, possibly through the introduction of surface defects or heterogeneous charge transfer sites. Furthermore, the extrusion-synthesized sample reveals a distinct shoulder in the PL spectrum, which is absent in the hydrothermal sample. This spectral feature could indicate the presence of unique defect states or intermediate energy levels introduced during the mechanochemical synthetic process, potentially acting as active sites for the generation or stabilization of photogenerated electrons consumed by adsorbed O_2 that triggers the formation of superoxide, and therefore a more selective oxidation from the alcohol to the aldehyde.

3.5. Influence of solvent, recyclability and stability of CN/CDs composite materials

Despite the limitations of using scavengers, it is possible to identify potential improvements in activity by using solvents that commonly favour the generation of radicals identified as more relevant. The catalytic activity was evaluated using acetonitrile as a solvent (A) and a 50/50 mixture of acetonitrile and water (W/A). Acetonitrile, being a polar aprotic solvent, can stabilize reactive intermediates such as $O_2^{\bullet-}$, which is crucial in the oxidation of alcohols to aldehydes. Furthermore, the solubility of O_2 in organic solvent is enhanced if compared to water,[59] consequently boosting the formation of $O_2^{\bullet-}$. The results presented in Fig. 10A show that the activity reaches a similar value, expressed as quantum efficiency, using water, acetonitrile or the water/acetonitrile mixture. However, selectivity towards benzaldehyde is optimized when acetonitrile is used. This can be explained by the fact that acetonitrile minimizes the formation of unselective radicals leading to the production of benzaldehyde.[60,61] Additionally, acetonitrile can interact more effectively with CN,

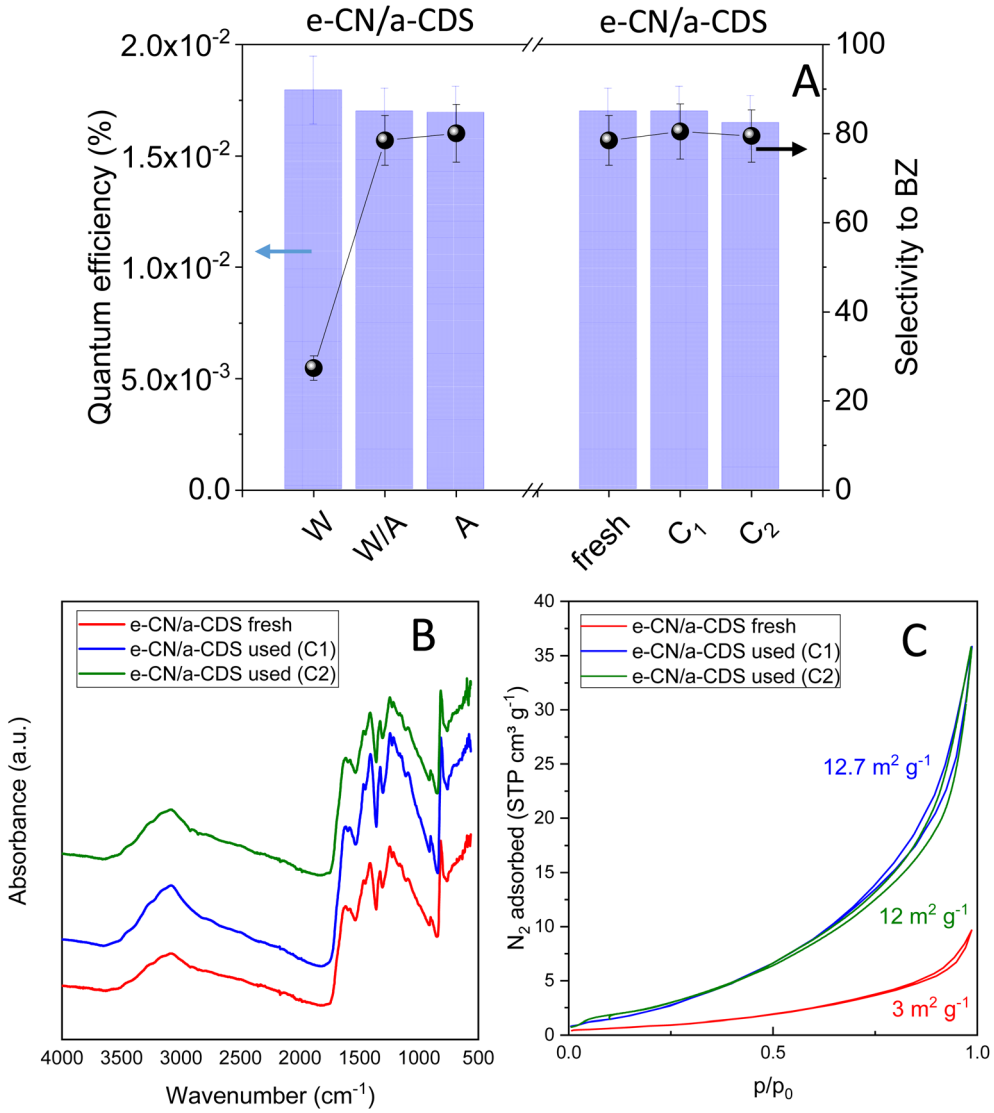

Fig. 10 (A) Influence of used solvent (W: water, W/A: 50/50 v/v water/acetonitrile, A: acetonitrile) using the e-CN/a-CDS composite sample, (B) FT-IR spectra of the fresh sample and after two reaction cycles (C1 and C2), (C) N_2 adsorption–desorption isotherms of the fresh sample and after two reaction cycles (C1 and C2).

improving the efficiency of electron transfer and, consequently, the selectivity of the process.

The stability and reusability of the e-CN/a-CDs sample have been evaluated as well. Structural, morphological, and optical stability were assessed using FT-IR, N_2 physisorption, and the determination of the photon absorption rate (differences between fresh and used samples below 1%), respectively (Fig. 10B and C). The main peaks that identify this structure include those corresponding to the stretching vibrations of C=N and C–N bonds, typically observed around 1200–1650 cm^{-1}. The results indicate a lack of significant changes in these peaks between the fresh and used samples, suggesting that the polymeric structure remains stable after use. While the structure of the sample remains practically unchanged, changes in morphology were detected. The BET area of the sample increased from 3 (fresh) to 12 (used) $m^2\ g^{-1}$. This increase in BET area can be attributed to the cleaning and re-activation of the pores within the sample. After this initial modification (C1), the morphology in terms of surface area and other porosity parameters remained constant. The samples are stable in terms of their optical properties, with a variation in the average photon absorption rate below 1%, indicating that the beneficial interaction between the CDS and the CN polymeric structure, described in previous sections, is maintained after several reaction cycles. This stability is also reflected in the reproducibility of the selective alcohol-to-aldehyde reaction. The quantum yield decreases slightly by 1% after two reaction cycles (C2), while the selectivity remains at ~80%.

4 Conclusions

In this study, we explored the development of sustainable, metal-free photocatalysts by synthesizing carbon dot-decorated graphitic carbon nitride composites through two distinct

methods - a hydrothermal approach and a solvent-free mechanochemical extrusion process. The choice of synthetic method played a crucial role in determining the structural, optical, and photocatalytic properties of the CN/CDs composites.

The similarity in LVRPA among different types of CDs within the same synthesis method underscores that the synthetic method is the predominant factor that define the photon absorption characteristics of the CN/CDs composites and determines the material's overall structure and defect density, rather than the specific treatment of the CDs.

The observed higher reaction rates in mechanochemical samples with amorphous and dialyzed CDs were attributed to the increased structural defects and better interaction with the CN matrix, which enhance charge carrier dynamics. However, the lack of corresponding improvement in quantum efficiency suggests that merely having a higher photon absorption rate does not guarantee better photocatalytic performance. The hydrothermal samples, although having lower LVRPA, exhibit better quantum efficiency due to more favourable optical and surface chemistry characteristics. The optimization of optical absorption and surface properties is crucial for achieving high photocatalytic performance.

The photocatalytic oxidation of benzyl alcohol to benzaldehyde in CN/CDs composite systems is primarily governed by superoxide radicals. The hydrothermal sample exhibits an enhanced contribution, involved by superoxide and hydroxyl radicals, making it more active under OA conditions. LVRPA data further supports the hydrothermal sample's greater UV absorption capacity, aligning with its superior performance. The extrusion sample, e-CN/a-CDs, demonstrates a more extensive suppression of electron–hole recombination, as evidenced by the greater PL intensity reduction. The unique PL shoulder observed in the extrusion sample may be associated with defect-induced active sites that could impact the stability and reactivity of the radicals. This study highlights the influence of synthetic methods on photocatalytic efficiency, showcasing the potential of tuning ROS generation and electron–hole dynamics through mechanical or hydrothermal preparation techniques in CN/CDs composites.

The e-CN/a-CDs sample demonstrates excellent stability and reusability. The structural integrity of the polymeric CN framework remains intact, as evidenced by consistent FT-IR spectra between fresh and used samples. Morphologically, while there is an increase in BET surface area, it does not significantly impact catalytic performance. The optical properties of the samples are stable, with less than 1% variation in the average absorption rate, indicating sustained beneficial interactions between CDS and the polymeric structure. Furthermore, the catalytic performance remains robust, with only a 2% decrease in quantum yield after two reaction cycles and consistent selectivity within the specified range. These findings underscore the sample's potential for long-term application in selective alcohol-to-aldehyde conversion reactions.

Data availability

All relevant data are within the manuscript and its ESI.†

Conflicts of interest

There are no conflicts to declare.

Acknowledgements

This project has received funding from the European Union's Horizon2020 research and innovation programme under the Marie Sklodowska-Curie Cofund Grant Agreement No. 945361 and the project PID2022-139014OB-I00/SRA (State Research Agency)/10.13039/501100011033.501100011033. Funding for open access charge: Universidad de Granada/CBUA.

References

1 Z. Kang and S. T. Lee, *Nanoscale*, 2019, **11**, 19214–19224.
2 S. N. Baker and G. A. Baker, *Angew. Chem. Int. Ed.*, 2010, **49**, 6726–6744.
3 P. Zuo, X. Lu, Z. Sun, Y. Guo and H. He, *Microchim. Acta*, 2016, **183**, 519–542.
4 X. T. Zheng, A. Ananthanarayanan, K. Q. Luo and P. Chen, *Small*, 2015, **11**, 1620–1636.
5 D. Rodríguez-Padrón, M. Algarra, L. A. C. Tarelho, J. Frade, A. Franco, G. De Miguel, J. Jiménez, E. Rodríguez-Castellón and R. Luque, *ACS Sustain. Chem. Eng.*, 2018, **6**, 7200–7205.
6 C. Xia, S. Zhu, T. Feng, M. Yang and B. Yang, *Adv. Sci.*, 2019, **6**, 1901316.
7 G. A. M. Hutton, B. C. M. Martindale and E. Reisner, *Chem. Soc. Rev.*, 2017, **46**, 6111–6123.
8 Y. Park, Y. Kim, H. Chang, S. Won, H. Kim and W. Kwon, *J. Mater. Chem. B*, 2020, **8**, 8935–8951.
9 S. Cailotto, R. Mazzaro, F. Enrichi, A. Vomiero, M. Selva, E. Cattaruzza, D. Cristofori, E. Amadio and A. Perosa, *ACS Appl. Mater. Interfaces*, 2018, **10**, 40560–40567.
10 Z. Zhu, Y. Zhai, Z. Li, P. Zhu, S. Mao, C. Zhu, D. Du, L. A. Belfiore, J. Tang and Y. Lin, *Mater. Today*, 2019, **30**, 52–79.
11 D. Rodríguez-Padrón, A. R. Puente-Santiago, A. M. Balu, M. J. Muñoz-Batista and R. Luque, *ChemCatChem*, 2019, **11**, 18–38.
12 J. C. Colmenares, R. Luque, J. M. Campelo, F. Colmenares, Z. Karpiński and A. A. Romero, *Materials*, 2009, **2**, 2228–2258.
13 S. Cailotto, M. Negrato, S. Daniele, R. Luque, M. Selva, E. Amadio and A. Perosa, *Green Chem.*, 2020, **22**, 1145–1149.
14 C. Campalani and D. Rigo, *Next Sustain.*, 2023, **1**, 100001.
15 B. Bin Chen, M. L. Liu and C. Z. Huang, *Green Chem.*, 2020, **22**, 4034–4054.
16 W. J. Ong, L. L. Tan, Y. H. Ng, S. T. Yong and S. P. Chai, *Chem. Rev.*, 2016, **116**, 7159–7329.
17 M. Han, S. Zhu, S. Lu, Y. Song, T. Feng, S. Tao, J. Liu and B. Yang, *Nano Today*, 2018, **19**, 201–218.
18 H. Yu, Y. Zhao, C. Zhou, L. Shang, Y. Peng, Y. Cao, L. Z. Wu, C. H. Tung and T. Zhang, *J. Mater. Chem. A*, 2014, **2**, 3344–3351.
19 X. Han, Y. Han, H. Huang, H. Zhang, X. Zhang, R. Liu, Y. Liu and Z. Kang, *Dalton Trans.*, 2013, **42**, 10380–10383.

20 H. Zhang, H. Huang, H. Ming, H. Li, L. Zhang, Y. Liu and Z. Kang, *J. Mater. Chem.*, 2012, **22**, 10501–10506.
21 H. Zhang, H. Ming, S. Lian, H. Huang, H. Li, L. Zhang, Y. Liu, Z. Kang and S. T. Lee, *Dalton Trans.*, 2011, **40**, 10822–10825.
22 H. Zhang, L. Zhao, F. Geng, L. H. Guo, B. Wan and Y. Yang, *Appl. Catal. B Environ.*, 2016, **180**, 656–662.
23 M. J. Muñoz-Batista, D. Rodriguez-Padron, A. R. Puente-Santiago and R. Luque, *ACS Sustain. Chem. Eng.*, 2018, **6**, 9530–9544.
24 H. Awang, T. Peppel and J. Strunk, *Catalysts*, 2023, **13**, 735.
25 N. Serpone, *J. Photochem. Photobiol., A*, 1997, **104**, 1–12.
26 O. Fontelles-Carceller, M. J. Muñoz-Batista, J. C. Conesa, A. Kubacka and M. Fernández-García, *Mol. Catal.*, 2018, **446**, 88–97.
27 M. A. Quintana, R. R. Solís, G. Blázquez, M. Calero and M. J. Muñoz-Batista, *Appl. Surf. Sci.*, 2024, **656**, 159717.
28 U. Caudillo-Flores, M. J. Muñoz-Batista, J. A. Cortés, M. Fernández-García and A. Kubacka, *Mol. Catal.*, 2017, **437**, 1–10.
29 H. Kaur, S. Kumar, P. Kumar, A. A. Ghfar and G. Bouzid, *Environ. Res.*, 2024, **259**, 119534.
30 O. Trentin, D. Ballesteros-Plata, E. Rodríguez-Castellón, L. Puppulin, M. Selva, A. Perosa and D. Rodriguez-Padron, *ChemSusChem*, 2024, e202401255.
31 M. Thommes, K. Kaneko, A. V. Neimark, J. P. Olivier, F. Rodriguez-Reinoso, J. Rouquerol and K. S. W. Sing, *Pure Appl. Chem.*, 2015, **87**, 1051–1069.
32 Z. A. Alothman, *Materials*, 2012, **5**, 2874–2902.
33 K. S. W. Sing, D. H. Everett, R. A. W. Haul, L. Moscou, R. A. Pierotti, J. Rouquerol and T. Siemieniewska, *Pure Appl. Chem.*, 1985, **57**, 603–619.
34 D. Wang, C. Shi, Z. Wu, J. Xiao, Z. Huang and Z. Fang, *Constr. Build. Mater.*, 2015, **96**, 368–377.
35 F. Bertella, P. Concepción and A. Martínez, *Catal. Today*, 2017, **296**, 170–180.
36 M. Santiago, J. C. Groen and J. Pérez-Ramírez, *J. Catal.*, 2008, **257**, 152–162.
37 D. Song and J. Li, *J. Mol. Catal. A:Chem.*, 2006, **247**, 206–212.
38 B. M. Amos-Tautua, O. J. Fakayode, S. P. Songca and O. S. Oluwafemi, *Nano-Struct. Nano-Objects*, 2020, **23**, 100480.
39 M. J. Muñoz-Batista, O. Fontelles-Carceller, A. Kubacka and M. Fernández-García, *Appl. Catal. B Environ.*, 2017, **203**, 663–672.
40 C. Kosanović, A. Čižmek, B. Subotić, I. Šmit, M. Stubičar and A. Tonejc, *Zeolites*, 1995, **15**, 51–57.
41 S. L. Madaswamy, S. M. Wabaidur, M. R. Khan, S. C. Lee and R. Dhanusuraman, *Macromol. Res.*, 2021, **29**, 411–417.
42 E. B. Chubenko, N. M. Denisov, A. V. Baglov, V. P. Bondarenko, V. V. Uglov and V. E. Borisenko, *Cryst. Res. Technol.*, 2020, **55**, 1900163.
43 M. J. Muñoz-Batista, M. Fernández-García and A. Kubacka, *Appl. Catal. B Environ.*, 2015, **164**, 261–270.
44 Y. Duan, S. Zhou, L. Deng, Z. Shi, H. Jiang and S. Zhou, *J. Environ. Chem. Eng.*, 2020, **8**, 104612.
45 S. Fang, Y. Xia, K. Lv, Q. Li, J. Sun and M. Li, *Appl. Catal. B Environ.*, 2016, **185**, 225–232.
46 R. M. Yadav, R. Kumar, A. Aliyan, P. S. Dobal, S. Biradar, R. Vajtai, D. P. Singh, A. A. Martí and P. M. Ajayan, *New J. Chem.*, 2020, **44**, 2644–2651.
47 M. J. Muñoz-Batista, M. M. Ballari, A. Kubacka, O. M. Alfano and M. Fernández-García, *Chem. Soc. Rev.*, 2019, **48**, 637–682.
48 U. Caudillo-Flores, M. J. Muñoz-Batista, M. Fernández-García and A. Kubacka, *Catal. Rev. - Sci. Eng.*, 2024, **66**, 531–585.
49 M. A. Quintana, J. Aguirre, M. Á. Martín-Lara, M. Calero, M. J. Muñoz-Batista and R. R. Solís, *Sustainable Mater. Technol.*, 2024, **42**, e01123.
50 S. Asadzadeh-Khaneghah and A. Habibi-Yangjeh, *J. Clean. Prod.*, 2020, **276**, 124319.
51 Y. Zhang, C. Shen, X. Lu, X. Mu and P. Song, *Spectrochim. Acta, Part A*, 2020, **227**, 117687.
52 Y. Nakayasu, Y. Goto, Y. Katsuyama, T. Itoh and M. Watanabe, *Carbon Trends*, 2022, **8**, 100190.
53 M. J. Muñoz-Batista, A. Kubacka, A. B. Hungría and M. Fernández-García, *J. Catal.*, 2015, **330**, 154–166.
54 K. Akbar, E. Moretti and A. Vomiero, *Adv. Opt. Mater.*, 2021, **9**, 2100532.
55 M. Pelaez, P. Falaras, V. Likodimos, K. O'Shea, A. A. de la Cruz, P. S. M. Dunlop, J. A. Byrne and D. D. Dionysiou, *J. Mol. Catal. A:Chem.*, 2016, **425**, 183–189.
56 R. Zandipak, N. Bahramifar, M. Torabi, M. Calero, M. J. Muñoz-Batista and R. R. Solís, *Chem. Eng. J.*, 2024, **494**, 152843.
57 E. M. Rodríguez, G. Márquez, M. Tena, P. M. Álvarez and F. J. Beltrán, *Appl. Catal. B Environ.*, 2015, **178**, 44–53.
58 P. M. Wood, *Biochem. J.*, 1988, **253**, 287–289.
59 J. Tripathy, G. Loget, M. Altomare and P. Schmuki, *J. Nanosci. Nanotechnol.*, 2016, **16**, 5353–5358.
60 M. A. Quintana, A. Picón, M. Á. Martín-Lara, M. Calero, M. J. Muñoz-Batista and R. R. Solís, *Appl. Catal., A*, 2024, **674**, 119607.
61 M. Alejandra Quintana, R. R. Solís, M. Ángeles Martín-Lara, G. Blázquez, F. Mónica Calero and M. J. Muñoz-Batista, *Sep. Purif. Technol.*, 2022, **298**, 121613.

